Journal of Chromatography A 1759 (2025) 466221

Contents lists available at ScienceDirect

Journal of Chromatography A

journal homepage: www.elsevier.com/locate/chroma

Comparison of stochiometric and colloidal adsorption models for mechanistic modeling of *parvovirus* clearance by anion exchange chromatography

Lukas Döring [a,b], Johannes Winderl [a], Marc Müller [a], Matthias W Kron [a], Jürgen Hubbuch [b,*]

[a] *Process Science, Rentschler Biopharma SE, Erwin-Rentschler-Str. 21, 88471 Laupheim, Germany*
[b] *Karlsruhe Institute of Technology (KIT), Institute of Engineering in Life Sciences, Section IV: Biomolecular Separation Engineering, Fritz-Haber-Weg 2, 76131 Karlsruhe, Germany*

ARTICLE INFO

Keywords:
Viral clearance
Mechanistic chromatography modeling
Anion exchange chromatography
Minute virus of mice
MVM
MVM mock virus particle
MVP
Colloidal particle adsorption
CPA
steric mass action
SMA
parvovirus

ABSTRACT

Anion exchange chromatography (AEX) is one of the downstream unit operations that is most frequently claimed for its capability to remove viruses. However, the impact of various process parameters on virus removal by AEX is still not fully understood. Mechanistic modeling could be a promising way to approach this knowledge gap. These models leverage physical and chemical principles to simulate a wide range of experimental conditions based on a limited number of wet lab calibration experiments. Especially the reduced need for resource-intensive virus spiking studies makes them a valuable tool to improve mechanistic understanding of viral clearance *in silico*.

We compared a stoichiometric and a colloidal adsorption model of parvoviral mock virus particles (MVP) on Q Sepharose FF to assess their abilities to predict LRVs of MVP over a pH range from 6.1 – 7.7 and sodium chloride concentrations from 0 – 400 mM. A general rate column model including pore diffusion was applied based on the finding that MVP can access ~3 % of the pore volume. While the stoichiometric model needed three pH-dependent parameters to describe the pH range, we were able to calibrate a colloidal model with only the charge being pH-dependent. Validation at the edge-of-failure showed good and comparable predictive power for both models. The colloidal particle adsorption (CPA) model showed a better fit to a validation dataset generated with process intermediates containing mAbs at higher volumetric loads. Since no residual MVPs were detected at low ionic strength (e.g. < 140 mM NaCl at pH 6.1 or < 220 mM NaCl at pH 7.7) the behavior of the adsorption models at these conditions could not be verified.

This study contributes to the applicability of *in silico* methods to virus removal by AEX and could aid knowledge-based platform validation of virus clearance by chromatographic methods.

1. Introduction

Biopharmaceuticals like monoclonal Antibodies (mAb) and other protein formats have experienced a constantly growing market share in the past years [1,2]. This growth was accompanied by raising competition and the need to reduce manufacturing costs. One of the key cost factors in biomanufacturing is downstream processing, which is a complex sequence of chromatography, filtration, and conditioning steps [3]. From an mechanistic perspective these unit operations are based on mass transport (convection, film diffusion, pore diffusion) and thermodynamics (adsorption), which can be described by ordinary differential equations or partial differential equations [4]. In the past years, academic and industrial efforts led to predictive mechanistic models of unit operations like affinity [5,6], anion exchange (AEX) [7], mixed mode (MM) [8,9] and cation exchange (CEX) [10,11] chromatography as well as ultrafiltration/diafiltration [11,12]. These models, based on physical and chemical principles, can simulate process behavior within a broad range of experimental conditions while minimizing the need for extensive wet lab experiments and can be connected to mechanistic process models capable of simulating whole process trains [13].

* Corresponding author at: Fritz-Haber-Weg 2, 76131 Karlsruhe, Germany.
E-mail address: juergen.hubbuch@kit.edu (J. Hubbuch).

https://doi.org/10.1016/j.chroma.2025.466221
Received 4 April 2025; Received in revised form 11 July 2025; Accepted 13 July 2025
Available online 15 July 2025

Biopharmaceuticals are often produced in Chinese hamster ovary (CHO) cell cultures. CHO cells are known to contain (type-A) and release (type-C) retrovirus-like particles (RVLPs), and there have been several reports of cell cultures infected by adventitious viruses [14]. Therefore, regulatory guidelines (ICH Q5A) require viral clearance for clinical and commercial use of biopharmaceuticals produced in these cell cultures [15–17]. The increasing availability of methodologies using non-infectious RVLP and minute virus of mice mock virus particles (MVP) in combination with molecular methods [18–21] enable investigation of virus clearance at reasonable cost and throughput [20, 22–26]. Especially the understanding of virus clearance by AEX chromatography was aided by these methodologies and support recent findings in understanding the impact of process parameters, the effect of surface charge distribution of viruses and virus mAb interactions [22, 27–30]. More recently, these findings led to efforts to describe virus removal of AEX chromatography using mechanistic modeling. These models have been shown to be valuable for better understanding of the impact of process parameters and to define the edge-of-failure of virus removal. However, due to the challenge of accurately describing chromatographic behavior on the $\log_{10}$-scale, calibrating these models required either analysis of a large number of fractions [31] or resulted in significant uncertainty of the model [32]. High analytical efforts make the calibration of these models less reasonable from a cost benefit standpoint especially, when costly studies with infectious viruses are performed. On the other hand, high uncertainty limits the application of these models for process design based on quality by design (QbD) principles. Further, these models were based on a steric mass action (SMA) adsorption model. SMA is based on an intuitive stoichiometric derivation of the electrostatic interaction between adsorber surfaces and biomolecules [33]. Non- stoichiometric colloidal particle adsorption (CPA) models recently gained more interest due to their ability to provide a better description over broad pH ranges, easier transferability between resins and better description of the behavior at high load conditions. These models follow a more fundamental approach and make use of the linearized Poisson Boltzmann equation to describe the electrostatic interaction between adsorber surfaces and biomolecules [34–37].

In this study, we compared a SMA and a CPA adsorption model for their capability to accurately predict the virus removal of MVP in AEX chromatography in flow through mode over a broad pH range (6.1 – 7.7). Based on the finding that MVP access a fraction of the Q Sepharose FF (QSFF) pores, a General Rate Model (GRM) column model was used. To obtain models with high confidence and reduced analytical effort, the calibration was performed with a straightforward dataset consisting of three linear gradient elution (LGE) and an incremental step elution (ISE) experiment at five pH values. The models were subsequently validated to accurately predict logarithmic reduction values (LRV) at the edge-of-failure at four pH values and various counter ion concentrations using an MVP spiked multi component buffer system (MCBS). After buffer validation, the mechanistic models were validated using process intermediates of three different monoclonal antibodies (mAbs) at extended volumetric loads. Finally, simulations were conducted to understand the impact and interaction of pH, ionic strength and volumetric load on the LRV of QSFF in flowthrough mode.

2. Theory

2.1. Column and system model

General Rate Models (GRM) include pore diffusion $D_{pore,i}$ as well as film mass transfer $k_{film,i}$. Therefore, GRMs are particularly useful in describing chromatography processes where proteins access the pore volume and where mass transfer as well as slow diffusion becomes limiting. Eq. (1) describes the GRM where the temporal change in concentration of the i th solute is dependent on convective mass transport driven by volumetric flow with the interstitial velocity u_{int}. The interstitial velocity is described by $u_{int} = u_{lin} / \varepsilon_b$ with u_{lin} beeing the linear flow rate and ε_b is the interstitial porosity. The axial dispersion coefficient D_{ax} describes the peak broadening effects. The model is complemented by Danckwerts boundary conditions in Eq. (2) and (3) with $c_{in,i}(t)$ being the concentration of the i th solute at the column inlet.

$$\frac{\partial c_i}{\partial t}(x,t) = -u_{int}\frac{\partial c_i}{\partial x}(x,t) + D_{ax}\frac{\partial^2 c_i}{\partial x^2}(x,t) - \frac{1-\varepsilon_b}{\varepsilon_b}\frac{3}{r_p}k_{film,i}\left(c_i - c_{p,i}(r=r_p)\right) \tag{1}$$

$$\frac{\partial c_i}{\partial t}(0,\ t) = \frac{u_{int}(t)}{D_{ax,\ i}}\left(c_i(0,\ t) - c_{in,i}(t)\right) \tag{2}$$

$$\frac{\partial c_i}{\partial t}(L,\ t) = 0 \tag{3}$$

The pore diffusion $D_{pore,i}$ is described in Eq. (4) with the particle porosity ε_p and $c_{p,i}$ being the protein concentration inside the pores of the resin particle. Modeling $D_{pore,i}$ requires the introduction of a radial coordinate $r \in (0, r_p)$, with r_p beeing the particle radius. The pore model is complemented by the symmetry condition at the particle center ($r = 0$) Eq. (5) and flux continuity at the particle surface ($r = r_p$) Eq. (6).

$$\frac{\partial c_{p,i}}{\partial t}(x,r,t) = D_{pore,\ i}\left(\frac{\partial^2 c_p}{\partial r^2} + \frac{2}{r}\frac{\partial c_p}{\partial r}\right) - \frac{1-\varepsilon_p}{\varepsilon_p}\frac{\partial q}{\partial t}(x,r,t) \tag{4}$$

$$\frac{\partial c_{p,i}}{\partial t}(x,r_p,t) = \frac{k_{film,\ i}}{\varepsilon_p D_{pore,i}}\left(c_i - c_{p,i}\right) \tag{5}$$

$$\frac{\partial c_{p,i}}{\partial t}(x,0,t) = 0 \tag{6}$$

2.2. Adsorption models

There are different ways to describe the adsorption mechanism of the virus onto the adsorber surface of an AEX chromatography resin. The SMA model describes the adsorption process as reversible equilibrium reaction. The assumption is that the formation of the protein-ligand complex can be expressed based on the law of mass action thereby considering only charges that are directly involved in the complex [33]. Although this is a practical and straightforward derivation, such stoichiometric models assume short-range interactions and are therefore non ideal for the description of the long-range interactions between proteins and AEX surfaces. To address this, colloidal models have been developed based on the linearized Poisson-Boltzmann equation. These models assume proteins as perfect spheres and the adsorber as a planar surface, both with uniform charge distribution, in an electrolyte solution. Using this non stoichiometric approach, the partitioning between both components is calculated based on the minimum free interaction energy in the interaction boundary layer [38–40]. Both models are schematically shown in Fig. 1 and described in detail in the following sections.

2.2.1. Steric mass action model

The steric mass action (SMA) isotherm describes the adsorption of molecules on a charged surface as a competitive equilibrium between the concentrations of adsorbed proteins per skeleton volume $q_{v,\ i}$ and liquid phase $c_{p,i}$ and the salt concentration c_s using a stochiometric approach. The characteristic charge ν depicts the number of functional groups that participate at the protein-ligand complex. Steric shielding factor σ describes the additional number of functional groups sterically masked by the adsorbed protein. The resins total ionic capacity is described by Λ [33]. A kinetic form of the SMA (Eq. (7)) was used, which describes the adsorption rate k_{ads} and desorption rate k_{des} of the i th solute as $k_{eq,i} = k_{ads,i}/k_{des,i}$ and $k_{kin,i} = 1/k_{des,i}$ respectively [41].

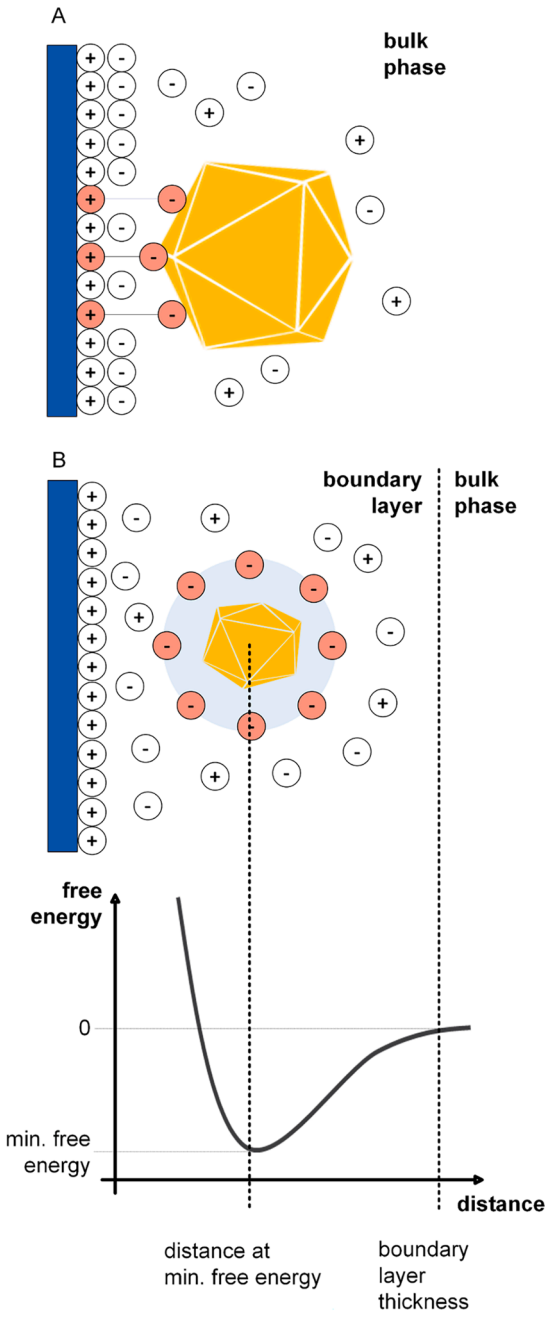

Fig. 1. Schematic representation of the foundational assumptions made by the steric mass action (SMA) model and the colloidal particle adsorption (CPA) model. The SMA follows a stoichiometric approach and describes the characteristic charge based on the number of charges that participate at the virus-ligand complex. The CPA describes the adsorption based on the interaction free energy affected by the electrostatic potential, assuming the virus as a perfect sphere with equally distributed charge.

$$k_{kin,\ i}\frac{\partial q_{v,i}}{\partial t} = k_{eq,\ i}\left(\Lambda - \sum_{j=1}^{k}(\nu_j + \sigma_j)q_j\right)^{\nu_i} c_{p,i} - q_i c_s^{\nu_i} \tag{7}$$

$$q_{salt} = \Lambda - \sum_{j=1}^{k}\nu_j q_j \tag{8}$$

Based on *Hunt* et al. the pH dependence of k_{eq}, and k_{kin} were described using exponential functions (Eqs. 9 and 10), while ν was described with a linear regresion model (Eq. 11) [42].

$$k_{eq,\ i}(pH) = k_{eq0,i}\ e^{k_{eq1,i}\ (pH - pH_{ref})} \tag{9}$$

$$k_{kin,i}(pH) = k_{kin0,i}\ e^{k_{kin1,\ i}\ (pH - pH_{ref})} \tag{10}$$

$$\nu_i(pH) = \ \nu_{0,i} + \nu_{1,i}\ (pH - pH_{ref}) \tag{11}$$

2.2.2. Colloidal particle adsorption model

The colloidal particle adsorption (CPA) developed by Briskot et al. [34–36] was used in this study. In the following sections the main elements of the model are summarized. For further details the reader is referred to the papers of Briskot et al..

Eq. (12) describes the CPA with $K_{v,i}$ being the equilibrium coefficient, while $q_{v,i}$ represents the adsorbed protein per skeleton volume of the adsorbent and $c_{p,i}$ denotes the protein concentration inside the boundary layer of the adsorber.

$$\frac{\partial q_{v,i}}{\partial t} = k_{kin,i}\left(K_{v,i}c_{p,i} - q_{v,i}\right) \tag{12}$$

As shown in Eq. (13) the kinetic $k_{kin,i}$ of the CPA model is not constant but dependent on the fitting parameter $k^*_{kin,i}$ and the characteristic minimum of interaction free energy $u_{A,i}(\delta_{m,i})$. Since $u_{A,i}(\delta_{m,i})$ is regulated by the protein charge Z_i and ionic strength I_m. These parameters also affect $k_{kin,i}$. k_b denotes the Boltzmann constant and T the temperature.

$$k_{kin,i} = k^*_{kin,i}\frac{1}{2}\left(\frac{u_{A,i}(\delta_{m,i})}{k_b T}\right)^2 \frac{1}{\cosh\left(\frac{u_{A,i}(\delta_{m,i})}{k_b T}\right) - 1} \tag{13}$$

The definition of the equilibrium coefficient $K_{v,i}$ is given in Eq. (14). The fitting parameter $\mathbf{\Delta_i}$ represents the boundary layer thickness at the resin surface and $B_i(\Theta)$ is the available surface function in dependence of the surface coverage Θ, while $u_{lat,i}$ being the lateral interaction energy between the proteins in the adsorption layer.

$$K_{v,i} = \Delta_i\frac{k_b T}{u_{A,i}(\delta_{m,i})}B_i(\Theta)exp\left(-\frac{u_{lat,i}}{k_b T}\right)\left(1 - \exp\left(-\frac{u_{A,i}(\delta_{m,i})}{k_b T}\right)\right) \tag{14}$$

$B_i(\Theta)$ is referred to as the available surface function (Eq. (15)), where Θ represents the surface coverage (Eq. (16)), N_A being the Avogadro number and q_i representing the protein adsorbed per adsorber surface.

$$B_i(\Theta) = (1-\Theta)exp\left(-\frac{\pi a_i^2\sum_i q_i N_A + 2\pi a_i\sum_i a_i q_i N_A}{(1-\Theta)} - \frac{\pi a_i^2\left(\sum_i a_i q_i N_A\right)^2}{(1-\Theta)^2}\right) \tag{15}$$

$$\Theta = \pi N_A\sum a_i^2\frac{q_{v,i}}{A_{s,i}} \tag{16}$$

At low load conditions, were $B_i(\Theta)$ and $u_{lat,i}$ are not limiting, $K_{v,i}$ can be reduced to Eq. (17).

$$K_{v,i} = \frac{\Delta_i k_b T}{u_{A,i}(\delta_{m,i})}\left(1 - \exp\left(-\frac{u_{A,i}(\delta_{m,i})}{k_b T}\right)\right) \tag{17}$$

The protein of interest is assumed to allocate in the interaction boundary layer at distance with the characteristic minimum of the interaction free energy $u_{A,i}(\delta_{m,i})$ defined in Eq. (18), within the boundary layer spatially limited by δ^*_i.

$$\delta_{m,i} = \underset{z}{\text{argmin}}u_{A,i}(z) \tag{18}$$

When both the adsorber surface and the protein approach each other a complex interaction profile between surface as a flat element and the protein as a curved element is expected. However, this complex interaction can be simplified using the Derjaguin approximation, which describes both the adsorber surface and the protein as planar surfaces interacting with each other and is applicable. Under the prerequisite of

the Derjaguin limit that $\kappa a_i \gg 1$. Via Eq. (19), the interaction free energy $u_{A,\,i}$ can be calculated from interaction free energy per area $w_{A,\,i}$, with z being the distance between adsorber surface and protein.

$$u_{A,i}(z) = 2\pi a_i \int_z^\infty w_{A,i}(z)\, dz \tag{19}$$

$w_{A,\,i}$ can be calculated from Eq. (20),

$$w_{A,i}(z) = \epsilon\epsilon_0\kappa \frac{2\psi_{0,A}\psi_{0,i}}{\exp(\kappa z) - \exp(-\kappa z)} + \epsilon\epsilon_0\kappa \frac{\left(\psi_{0,A}^2 + \psi_{0,i}^2\right)\exp(-\kappa z)}{\exp(\kappa z) - \exp(-\kappa z)} \tag{20}$$

considering the electrostatic surface potential at the adsorber surface $\psi_{0,A}$, the electrostatic surface potential at the protein $\psi_{0,i}$, and the inverse debye length κ Eq. (21) [35,43,44].

$$\kappa = \sqrt{\frac{2e^2 I_m N_A}{k_B T \varepsilon\varepsilon_0}} \tag{21}$$

With the relative permittivity of the surrounding electrolyte solution ε, the vacuum permittivity ε_0, and e denoting the elementary charge.

The electrostatic surface potentials of the protein and the adsorber surface can be described with the Gouy-Chapmann theory. According to this theory, the structure of an electric double layer the interface between a charged surface and an electrolyte solution consisting of an inner layer I with immobile ions and a diffusive layer D consisting of mobile ions, which are distributed according to electrostatic forces. The surface potential ψ_0 can be calculated assuming electroneutrality between the charge-potential of the inner layer $\sigma_I(\psi_0)$ and the diffusive layer $\sigma_D(\psi_0)$ (Eq. (22)).

$$\sigma_D(\psi_0) = \sigma_I(\psi_0) \tag{22}$$

Simplifying the systems towards planar surfaces according to the Derjaguin approximation, the charge density of the diffusive layer of the adsorber surface $\sigma_{D,\,A}(\psi_0)$ or the protein $\sigma_{D,\,i}(\psi_0)$ can be calculated via the Grahame relation (Eq. (23)) [45,46]

$$\sigma_D = 2\varepsilon\varepsilon_0\kappa k_B T \sinh\left(\frac{e\psi_0}{2k_B T}\right) \tag{23}$$

In contrast to the potential of the diffusive layer, the charge-potential ration of the inner layer the surface charge density of the adsorber surface $\sigma_{I,\,A}$ and the protein $\sigma_{I,\,i}$, have to be calculated in different ways. The surface charge density of the adsorber surface $\sigma_{I,\,A}$ can be derived from the dissociation reaction of the Ligand L occurring at the respective pKa

$$LH^{\zeta_L} \rightleftharpoons L^{\zeta_L - 1}\ H^+ \tag{24}$$

and can be described as a function of pH via Eq. (25), where ζ_L describes the ligand charge of either an anion exchanger ($\zeta_L = 1$) or a cation exchanger ($\zeta_L = 0$).

$$\sigma_{I,\,A} = eN_A\Gamma_L\left[\zeta_L - \left(1 + 10^{pK_L - pH_0}\right)^{-1}\right] \tag{25}$$

With Γ_L being the ligand surface density, which is dependent on the dissociation constat pK_L of the ligand and the local pH at the surface pH_0 as given in Eq. (26). pH_0 is defined by the Boltzmann relation with the bulk phase pH [35,46].

$$pH_0 = pH + \frac{1}{\ln(10)}\frac{e\psi_0}{k_B T} \tag{26}$$

Combining Eq. (25) and Eq. (26), $\sigma_{I,\,A}$ can be described as a function of the electrostatic potential $\sigma_{I,\,A}(\psi_0)$.

The surface charge density of the protein $\sigma_{I,\,i}$, is determined by charge Z_i of the protein (Eq. (27)), which depends on the protonation states of its exposed amino acid residues.

$$\sigma_{I,\,i}(pH) = \frac{eZ_i(pH)}{4\pi a_i^2} \tag{27}$$

The pH dependence of Z_i can be approximated using a polynomial expression (Eq. (28)),

$$Z_i(pH) = Z_i\left(pH_{ref}\right) + \sum_{k=1}^{m} Z_{k,i}\left(pH - pH_{ref}\right)^k \tag{28}$$

where m represents the degree of the polynomial, $Z_{k,i}$ denotes the empirical parameters describing the titration curve, pH_{ref} denotes a reference pH value and $Z_i\left(pH_{ref}\right)$ represents the protein charge at the reference pH [34,35]. The degree of the polynomial required to describe Z_i in dependence of pH varies depending on the complexity of the protein's titration curve and the selected pH range.

In this paper the simplified CPA model (Eq. (17)) that neglects protein-protein interactions at the absorber surface was used. Therefore, we refer to Briskot et al. for a detailed derivation of the parameter $u_{lat,i}$ that takes account for these interactions [35].

3. Materials and methods

3.1. Resin, buffers and molecules

If not stated otherwise all chemicals were obtained from Merck (Darmstadt, Germany). The strong anion exchange chromatography resin QSFF (Cytiva, Marlborough, USA) was used in this study. The GRM model was calibrated using MiniChrom Prepacked columns (Repligen) with an inner diameter (d_c) of 8 mm and bed height (L_c) of 100 mm. Spiking MVP were obtained from Cygnus (Southport, USA).

Chromatography runs for calibration and validation were performed with a MCBS [31] with additional sodium chloride concentration of 20 or 1000 mM NaCl. All buffers were prepared with purified water, adjusted to the respective pH using 1 M sodium hydroxide or 1 M hydrochloric acid and filtered using 0.45/0.22 µm Sartopore 2 (Sartorius, Göttingen, Germany).

Monoclonal antibodies (mAbs) were produced in genetically engineered CHO expression systems using standard methods. The mAbs were captured from harvest cell culture fluid using protein A chromatography, neutralized to pH 6.0, depth filtered and stored at −70 °C. Before use, mAbs were thawed, dialyzed into MCBS using 30 mL Silde-A-Lyzer dialysis cassettes with 10 kDa cut off and adjusted to the respective protein concentration and ionic strength using the MCBS.

3.2. Instruments

Chromatographic experiments were performed using a ÄKTA Pure 25 system with a 10 mm UV flow cell and a F9-C fraction collector. The chromatography system was controlled with the Unicorn software version 7.10 (Cytiva, Marlborough, USA).

3.3. Software

Numerical simulations and parameter estimations were conducted using the GoSilico chromatography modeling software (GSCM) (Cytiva, Marlborough, USA). For all simulations, the columns were spatially divided into 15 axial and 5 radial cells of the same size. Temporal discretization employed a Crank-Nicolson time-stepping scheme with a step size of 5 s. Data visualization was performed using Python version 3.7.6. Contour plots were generated using the statistical software JMP 18.

3.4. System and column characterization

System dead volumes and mixing behavior of the chromatography

system were simulated as described previously [31]. Total porosity ε_t, interstitial porosity ε_b, and particle porosity ε_p were determined with 1 M sodium chloride pulse as pore penetrating tracer and MVP in 1 M sodium chloride as none pore penetrating tracer. The ionic capacity Λ was determined by on-column titration as described by Huuk et al. [47]. The film transfer k_{film} was calculated via the penetration theory correlation while the pore diffusion D_{pore} was calculated using the Mackie-Meares correlation [48,49].

To characterize the available surface of the MVP the inverse size exclusion chromatography (iSEC) method was used. It was assumed that the pore size distribution (PSD) follows a log-normal distribution given by $f(r)$ Eq. (29) with r_p being the mean pore size and s_p representing the standard deviation of the PSD.

$$f(r) = \frac{1}{r}\exp\left[-\frac{1}{2}\left(\frac{log\ (r/r_p)}{s_p}\right)^2\right] \tag{29}$$

For estimation of r_p and s_p, the K_d values of sodium chloride, differently sized dextrans and MVP were experimentally determined at 200 cm/h and fitted to Eq. (30) via the Nelder-Mead-Method, r_h denotes the hydrodynamic radius of the respective molecule.

$$K_d = \frac{\int_{r_m}^{\infty} f(r)\left[1-(r_h/r)^2\right]\mathrm{d}r}{\int_0^{\infty} f(r)\mathrm{d}r} \tag{30}$$

Subsequently, the PSD including the fitted r_p and s_p were used to calculate the accessible pore area per adsorber skeleton volume A_s, as described by DePhilips and Lenhoff (Eq. (31)) [50].

$$A_{s,i}(r_h) = \frac{\varepsilon_p}{1-\varepsilon_p}\frac{\int_{r_m}^{\infty} 2(r-r_h)r^{-2}f(r)\mathrm{d}r}{\int_0^{\infty} f(r)\mathrm{d}r} \tag{31}$$

For very small molecules the limiting case $A_{s,0} = lim_{r_m \to 0} A_{s,i}(r_m)$ defines the maximum accessible pore area per skeleton volume, which is necessary to calculate the ligand surface density Γ_L with regards to the ionic capacity (Eq. (32)).

$$\Gamma_L = \Lambda\, A_{S,0}^{-1} \tag{32}$$

All column characterization experiments were performed in triplicates.

3.5. Chromatography experiments and parameter estimation

For model calibration three LGE runs and one ISE run were performed at pH 6.1, 6.5, 7.1, 7.4, and 7.7. Blank runs with 1 % (v/v) PBS spike were performed for each run and the resulting UV traces were subtracted from the calibration runs before parameter estimation. As shown in Fig. 2, for initial calibration of the SMA parameters k_{eq} and ν, the UV traces of the LGE runs were analyzed using the Yamamoto correlation [51]. Subsequently k_{kin} was estimated while refining k_{eq} and ν by reversely fitting to UV traces and MVP immuno-qPCR offline data using a Levenberg-Marquart (LM) algorithm. CPA parameters Z, Δ and k^*_{kin} were reversely fitted to UV traces and MVP immuno-qPCR offline data using a two-stage calibration strategy. For initial estimation of the parameters an Adaptive Simulated Annealing (ASA) algorithm was used followed by further refinement applying an LM algorithm. After calibrating the model for each pH respectively the resulting parameters were plotted over the pH and fitted to the functions given in the theory section. Uncertainty of the model parameters was evaluated based on an estimate of the covariance matrix as previously described in Hahn et al. [6], using the GSCM software. For model validation flowthrough experiments were either performed using MVP-spiked MCBS (buffer validation) or mAb containing process intermediates spiked with MVP (mAb validation). All calibration and validation runs with their respective total MVP load, mAb load, volumetric load, objective, pH, and sodium chloride concentrations are shown in Table 1 and Table 2.

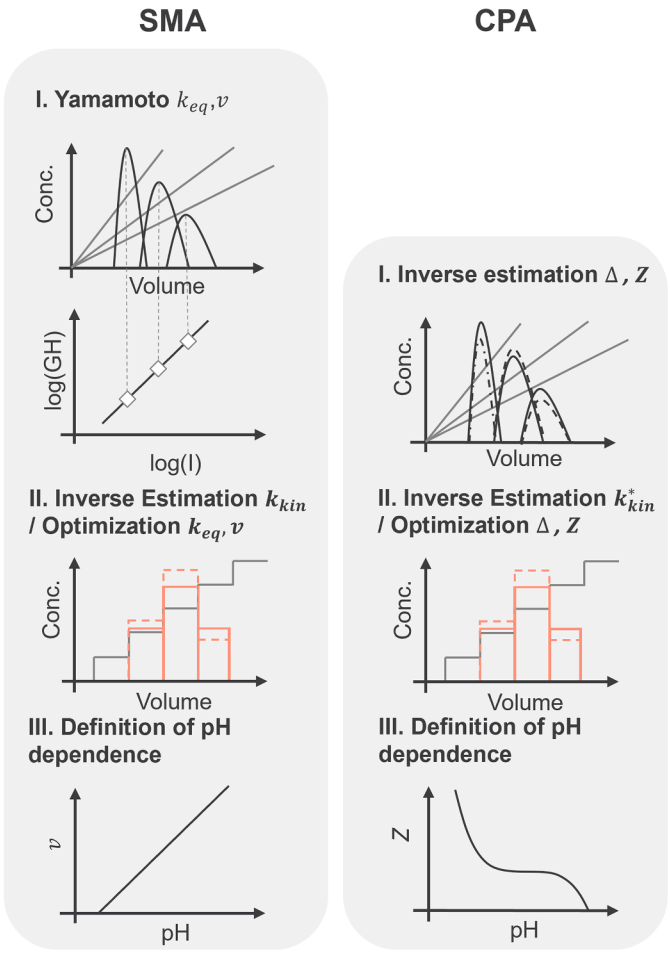

Fig. 2. Calibration strategies for Steric Mass Action (SMA) and Colloidal Particle Adsorption (CPA) model.

3.6. Virus surrogate quantification

MVP was analyzed using immuno-qPCR with the MockV® MVM Kit (Cygnus, Southport, USA). Quantification was performed following the vendor's instructions using a LightCycler® 480 II device (Roche).

4. Results and discussion

4.1. System and column characterization

The calibration and validation experiments described in this paper were run using a previously characterized chromatography system. Dead volumes, mixing and dispersive behavior were published in [31]. Column porosities were determined by sodium chloride and dextran pulses while the ionic capacity was determined using on-column titration. The pore accessibility was examined by inverse size exclusion chromatography (iSEC) for two reasons. Firstly, to make a profound decision, which column models including pore diffusion are a reasonable choice when it comes to modeling of *parvovirus* particles, and secondly, to estimate the theoretical surface area that is accessible to the MVP $A_{s,\ MVP}$. The iSEC experiments were run using six preparative dextrans and the MVP under non-adsorbing conditions. As shown in Fig. 3, the MVP used in this study was slightly retained by QSFF and showed a specific particle porosity ε_b, MVP of 0.027 resulting in the theoretical surface area per resin volume accessible for the MVP $A_{s,\ MVP}$ of 0.068 nm^{-1}. A total accessible surface area per resin volume $A_{s,\ 0}$ of 0.616 nm^{-1} was determined. All resulting column parameters are listed in Table 3.

Table 1
Summary of calibration experiments performed with different gradients, pH values and sodium chloride concentrations.

MVP Load [Particles]	Load volume [mL]	Objective	Elution mode	pH	NaCl conc. c_s [mM] Load / Equilibration / Wash	NaCl conc. c_s [mM] Elution	Gradient / Step length [CV]
10^{11}	5	Yamamoto method	LGE	6.1	20	20 – 1000	20, 40, 60
10^{11}	5	Inverse estimation	ISE	6.1	20	100 – 320	3
10^{11}	5	Yamamoto method	LGE	6.5	20	20 – 1000	20, 40, 60
10^{11}	5	Inverse estimation	ISE	6.5	20	100 – 320	3
10^{11}	5	Yamamoto method	LGE	7.1	20	20 – 1000	20, 40, 60
10^{11}	5	Inverse estimation	ISE	7.1	20	100 – 320	3
10^{11}	5	Yamamoto method	LGE	7.4	20	20 – 1000	20, 40, 60
10^{11}	5	Inverse estimation	ISE	7.4	20	100 – 320	3
10^{11}	5	Yamamoto method	LGE	7.7	20	20 – 1000	20, 40, 60
10^{11}	5	Inverse estimation	ISE	7.7	20	100 – 320	3

Table 2
Summary of validation experiments performed with different gradients, pH values and sodium chloride concentrations.

MVP Load [Particles]	mAb Load [g/L_{resin}]	Volumetric Load [mL]	Objective		pH	NaCl conc. c_s [mM] Load / Equilibration / Wash
10^{11}	–	5	Buffer Validation		6.1	20, 140, 160, 180
10^{11}	–	5			6.5	20, 180, 200, 220
10^{11}	–	5			7.1	20, 200, 220, 240
10^{11}	–	5			7.7	20, 220, 240, 260
10^{11}	30	25	mAb Validation	mAb1, mAb2,	6.5	20, 160, 180, 200
10^{11}	30	25		mAb3	7.4	20, 200, 220, 240

Based on the pore accessibility of the MVP it was assumed that GRM models, which include pore diffusion, are suitable for modeling of *parvovirus* particle adsorption on QSFF. The mass transfer parameters for the GRM were calculated according to the empiric correlations given in Table 4.

4.2. Model calibration

The aim of this study was to calibrate a mechanistic model that can predict the LRV of MVPs during QSFF based AEX in flowthrough mode over sodium chloride concentrations ranging from 20 – 500 mM and a pH range from 6.1 – 7.7. To calibrate SMA and CPA adsorption isotherms three LGE experiments, and one ISE run were performed with MVP spiked buffer.

In our previous study, we showed that particle loads typical for virus clearance studies can hardly become a limiting factor, assuming that particles are only adsorbed to the outer surface of chromatography beads [31]. This became even more evident when considering the pore accessibility of the MVP particle. A fractional surface area of 0.00034 % was calculated from the circular area of an MVP $A_{MVP} = \pi r_h^2 c_{MVP} V_{load}$ and the surface area accessible to the MVP. Therefore, the shielding factor σ of the SMA, as well as the available surface function $B_i(\Theta)$ and lateral interaction energy $u_{lat,i}$ of the CPA, were assumed to be negligible.

The parameters k_{eq} and ν for SMA (Eq. (7)) and Z and Δ for CPA (Eq. (17)) were initially estimated from UV signals of the LGE runs. ISEs were used to refine k_{eq} and ν as well as inverse estimation of the kinetic parameter k_{kin} based on UV signals and immuno-qPCR analysis.

After estimating the parameters of both adsorption models for each pH individually, they were fitted to the respective equations given in Section 2.2.1, to describe their pH dependencies. As shown in Fig. 4A-C, three pH dependent parameters k_{eq}, ν and k_{kin} were necessary to describe the MVP behavior at a pH range from 6.1 to 7.7 with the SMA model. The characteristic charge ν increased with increasing pH, while the equilibrium parameter k_{eq} became smaller. This behavior of k_{eq} appears counterintuitive since one would expect stronger adsorption of MVP to QSFF at higher pH values. A reasonable explanation for this behavior might result from a comparison with the CPA model. The CPA model could be described with electrostatic surface potential Z being the only pH dependent parameter (Fig. 4D). Z showed a non-linear behavior with a steep decrease between pH 6.1 and 6.5, probably caused by deprotonation of histidine side chains. This behavior was described using a third order polynomial consisting of Z_0, Z_1, Z_2 and Z_3. Considering this behavior of Z, the decreasing k_{eq} values of the SMA might be a compensation of the overestimated impact of the pH resulting from the linear expression of ν. While pH dependence of k_{eq} and ν has been reported previously, the kinetic parameter k_{kin} of the SMA is usually described as a pH independent parameter [42,52]. Due to the substantial changes of k_{eq}, a constant k_{kin} was not sufficient for the SMA model calibrated in this study. Since k_{eq} and k_{kin} are connected by $k_{eq} = k_{ads}/k_{des}$ and $k_{kin} = 1/k_{des}$ it was necessary to increase the desorption rate k_{des} leading to a pH dependent k_{kin}. Initial simulations without pH dependent k_{kin} led to pH dependent MVP breakthrough during load (data not shown), caused by compensation though a decreasing adsorption rate k_{ads}. The CPA model on the other hand, was expressed with constant values of Δ and k_{kin}^* over the calibrated pH range (Fig. 4E-F). The differences in the pH dependence of the SMA and CPA model might be attributed to the different mechanistic derivation. SMA characteristic charge ν only takes account for the number of ligands that are involved in the formation of the MVP-ligand complex, Z accounts for the electrostatic surface potential of the MVP and is not based on the interaction with the ligand. Apart from a reduced number of pH affected parameters when using the CPA, this might also enable the transfer of Z_i towards other resins, as previously described by Briskot et al. [35]. This resin transfer could significantly reduce the required experimental effort for calibration.

The 95 % CI of the SMA model parameters were smaller compared to the confidence of the calibrated CPA model. This was mainly caused by the higher confidence of the ionic strength independent k_{kin} of SMA, which was well suited to describe the maximum LRV. The pH dependent model parameters of both models are listed in Table 5.

As shown in Fig. 5, the UV profiles from the ISE calibration runs showed a series of minor UV peaks (< 10 mAu) during loading phase and the initial increment step. Since these fractions did not show positive

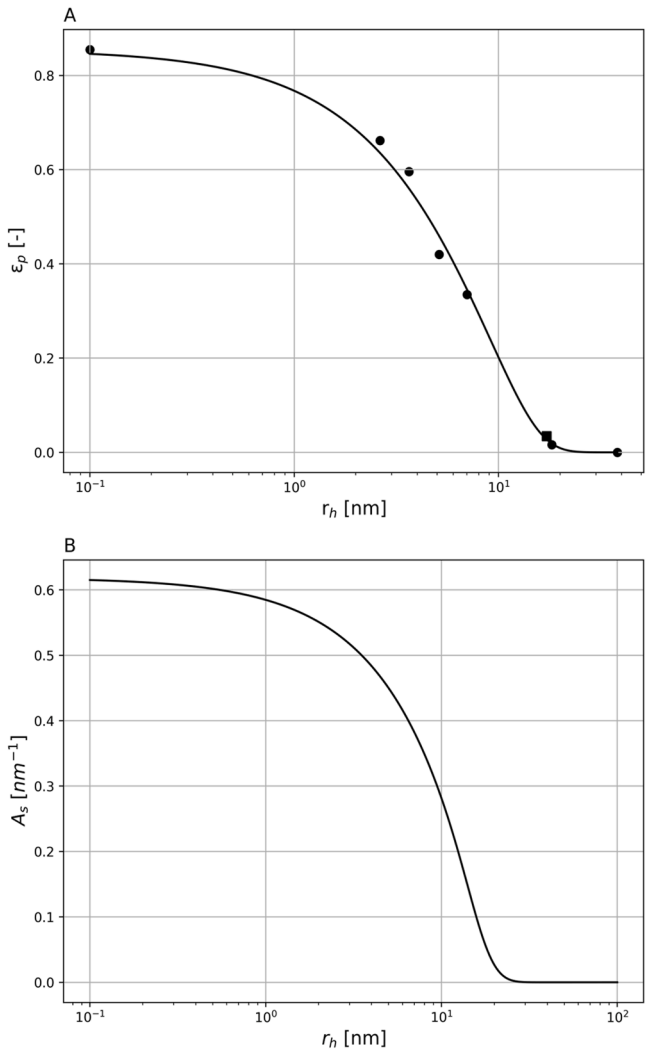

Fig. 3. Characterization of pore accessibility of QSFF by iSEC. (A) Specific porosities ε_b of dextrans (●) and MVP (■) and fitted pore model (-). (B) Accessible surface area in dependence of the hydrodynamic radius r_h.

Table 3
Column parameters, units, and sources.

Parameter	Symbol	Value	Unit	Source
Diameter	d_c	8	mm	Manufacturer
Length	L_c	100	mm	Manufacturer
Column volume	V_c	5.027	mL	$V_c = \pi\left(\frac{d_c}{2}\right)^2 L_c$
Bead radius	r_m	45	µm	Manufacturer
Total column porosity	ε_t	0.893	–	$\varepsilon_t = \frac{V_f}{V_c}$
Interstitial porosity	ε_b	0.262	–	$\varepsilon_b = \frac{V_{int}}{V_c}$
Particle porosity	ε_p	0.855	–	$\varepsilon_p = \frac{V_f - V_{int}}{V_c - V_{int}}$
Ionic capacity	Λ	2.02	M	$\Lambda = \frac{c_{Cl^-} V_{Cl^-}}{V_c(1-\varepsilon_t)}$
Accessible pore area salt	$A_{s,0}$	0.616	nm^{-1}	$A_{s,i}(r_h) = \frac{\varepsilon_p}{1-\varepsilon_p}\frac{\int_{r_m}^{\infty} 2(r-r_h)r^{-2}f(r)\mathrm{d}r}{\int_0^{\infty} f(r)\mathrm{d}r}$
Accessible pore area MVP	$A_{s,i}$	0.068	nm^{-1}	
Ligand density	Γ_L	3.58×10^{-6}	mol/m^2	$\Gamma_L = \Lambda A_{S,0}^{-1}$

Table 4
Mass transfer parameters of General Rate Model (GRM).

Parameter	Symbol	Value	Unit	Source
Axial dispersion	D_{ax}	2.5×10^{-7}	m^2/s	$D_{ax} = \frac{u_{int} 2r_{h,i}\varepsilon_{int}}{0.2 + 0.011(\varepsilon_{int} Re_p)^{0.48}}$
Hydrodynamic radius MVP	$r_{h,\ MVP}$	17.2	nm	[21]
Hydrodynamic radius Cl^-	$r_{h,s}$	0.12	nm	
Diffusion coefficient MVP	$D_{m,\ MVP}$	1.4×10^{-11}	m^2/s	$D_{m,i} = \frac{k_B T}{6\pi\eta r_{h,i}}$
Diffusion coefficient Cl^-	$D_{m,\ s}$	2.0×10^{-9}	m^2/s	
Film transfer MVP	$k_{film,\ MVP}$	4.3×10^{-6}	m/s	$k_{flim} = \frac{1.09}{\varepsilon_{int}}\frac{D_{m,i}}{2r_{h,i}}\left(\frac{\varepsilon_{int} u_{int} 2r_{h,i}}{D_{m,i}}\right)^{0.33}$
Film transfer Cl^-	$k_{film,\ s}$	1.2×10^{-4}	m/s	
Pore diffusion MVP	$D_{p,\ MVP}$	9.3×10^{-11}	m^2/s	$D_{pore,i} = \frac{\varepsilon_p}{(2-\varepsilon_p)^2} D_{m,i}$
Pore diffusion Cl^-	$D_{p,\ s}$	1.3×10^{-9}	m^2/s	

results in the immuno-qPCR analysis, the UV peaks are likely artefacts caused by buffer variations or trace impurities in the commercially obtained MVP. Consequently, they were not considered critical. The comparison of the calibrated adsorption models and experimental data showed that both the SMA and the CPA model successfully captured the onset of the MVP elution, as indicated by the UV signal and quantified on the logarithmic scale via Immuno-qPCR. The calibration experiments showed continued elution of low levels of MVP at ionic strengths where both models predicted complete elution of the MVP. This difference between models and calibration experiments might be caused by dependency of the molecular diffusion coefficient on ionic strength. In this study, D_{pore} of the MVP was approximated from the r_h using the Stokes-Einstein and Mackie-Meares equation, assuming the diffusion to be constant. In contrast, it is known that D_{pore} of proteins can be dependent on the ionic strength [53,54]. GRM that take account for ionic strength dependency of D_{pore} have been described in literature and could give a more detailed description of the MVP elution behavior, with the downside of increasing model complexity [55]. In general, the CPA model showed a higher degree of congruence with the calibration runs, both in terms of the number of elution peaks and continued elution of MVP at higher ionic strength. Since the onset of elution was accurately described by both models and considered to be more critical for predicting the edge-of-failure of virus removal, subsequent model validation was conducted for both models.

4.3. Validation in buffer

To verify the capability of the calibrated model to predict MVP removal over a broad range of pH values and ionic strength, flowthrough runs were simulated in 1 mM increments with sodium chloride concentration ranging from 0 to 400 mM at pH 6.1, 6.5, 7.1, and 7.7. Based on the predictions of the calibrated models, four flowthrough experiments per pH were performed with MVP spiked buffer to verify the model. One experiment at minimum sodium chloride concentration of 20 mM and three runs at sodium chloride concentrations close to the edge-of-failure, at which a declining LRV was expected.

At lower ionic strength, the behavior of the SMA and the CPA model showed a divergent behavior. SMA predicted a plateau at a maximum LRV of 4.9 at low ionic strength, while CPA predicted a constant decline of LRV until reaching the edge-of-failure (Fig. 6). When approaching the edge-of-failure both models predicted a comparable LRV decline. The differences in the prediction of LRV as a function of ionic strength are caused by the different mechanistic descriptions of both models. Under conditions where counter ions do not displace the bound MVP and mass transfer is not limiting, the only remaining restriction is the rate of

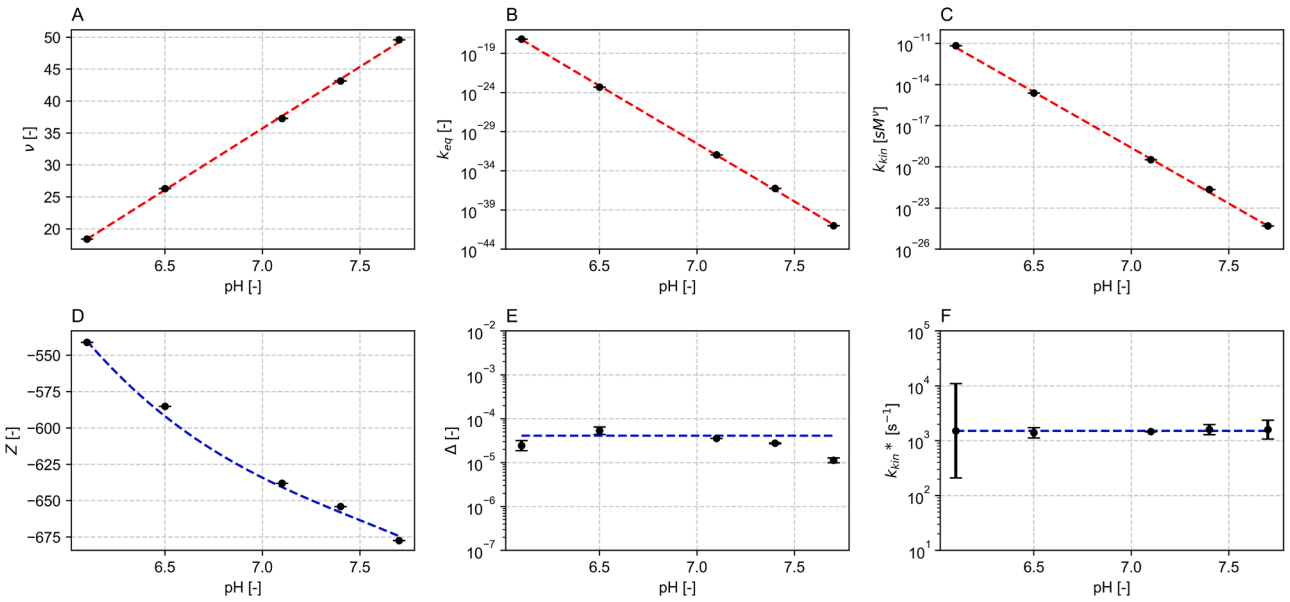

Fig. 4. pH dependance of the parameters $\boldsymbol{\nu}$ (A), $\boldsymbol{k_{eq}}$ (B), and $\boldsymbol{k_{kin}}$ (C) of the SMA adsorption model as well as $\boldsymbol{Z}$ (D), $\boldsymbol{\Delta}$ (E), and $\boldsymbol{k_{kin}}$* (F) of the CPA adsorption model. Dashed lines represent fitted parameter correlations. Error bars indicate the 95 % confidence interval of the respective parameters.

Table 5
SMA and CPA parameters of the pH dependent MVP model.

SMA Parameter	Symbol	Value	CPA Parameter	Symbol	Value
Characteristic charge [-]	ν_o	33.78	Charge [-]	Z_o	−656.7
	ν_1	19.27		Z_1	−54.81
				Z_2	6.850
				Z_3	−16.90
Equilibrium constant [-]	$k_{eq,0}$	9E-30	Boundary layer thickness [-]	Δ	4.12e-05
	$k_{eq,1}$	33.98			
Kinetic coefficient [sM^{σ}]	$k_{kin,\ 0}$	2E-18	Kinetic coefficient [s^{-1}]	k^*_{kin}	1510
	$k_{kin,\ 1}$	−18.72			
Reference pH	pH_{ref}	6.90	Reference pH	pH_{ref}	7.38

adsorption/desorption described by the kinetics k_{kin}. The SMA defines k_{kin} as a constant rate leading maximum LRV independent of the ionic strength (Eq. (7)). In contrast, the CPA defines k_{kin} as a function of the minimum interaction energy and thereby as a function of the ionic strength (Eq. (13)). Hence, a lower ionic strength leads to a lower degree of free energy, an increase in the adsorption/desorption rate, and thereby an increase in the maximal LRV. Both the SMA and the CPA model were calibrated on data that are restricted by the LOQ of the offline analytics used. Since no residual MVPs could be detected at low ionic strength (e.g. < 140 mM NaCl at pH 6.1 or < 220 mM NaCl at pH 7.7), the LRVs at values > 4 at these conditions have to be considered as non verified extrapolations. Therefore, we were not able to confirm which simulated behavior at lower ionic strength is more accurate. To verify the model predictions at low ionic strength, spiked MVP concentrations would have to be at least 1000x higher than those tested in this study. Such high MVP spikes were not possible to realize based on the concentration of the available material. For practical applications, this has minor consequences, as low ionic strength ensures high levels of virus removal. The LOQ in assays commonly used for virus clearance studies is primarily constrained by experimental parameters and the composition of buffer matrices, which can affect assay sensitivity. Based on literature values for QSFF (LRV ~ 5) the maximum LRV predicted at low ionic strength by the SMA model seems to be more likely [28]. Effective removal of viruses is typical for AEX chromatography low ionic strength and neutral pH [56]. Nevertheless, the predictions of the SMA and CPA at the edge-of -failure were verified and in good agreement validation runs. In general, both model types showed a similar behaviour close to the edge-of-failure and comparable Root Mean Square Error of Prediction (RMSEP) values of 0.36 for the SMA and 0.68 for the CPA. The slightly higher RMSEP of the CPA model was mainly caused by a poorer fit to the validation runs at LRV < 1.

4.4. *Validation in presence of mAb*

After validation of the mechanistic models in buffer matrices the next step was to increase the complexity and test the predictions in presence of three different mAbs (mAb1, mAb2, and mAb3), which were previously purified by protein A chromatography, low pH, and depth filtration. mAb validation runs were performed at four counter ion concentrations close to the edge-of-failure. pH 6.5 was chosen to compare validation in buffer with validation in presence of mAbs. pH 7.4 was chosen as a previously non-validated condition. Due to the target mAb load of 30 g_{mAb} L_{resin}^{-1} the validation runs in presence of mAbs, were performed and simulated with higher loading volumes of 25 mL compared to 5 mL for the buffer validation runs. Therefore, mAb validation runs were additionally used to validate the extrapolation of the models towards higher load volumina.

As shown in Fig. 7, the CPA adsorption model predicted a shallower curve that matched more closely to the measured data than the steep curve predicted by the SMA. This was also reflected by the higher RMSEP of the SMA compared to the CPA (Table 6). Both adsorption models predicted a decline in LRV at lower counter ion concentrations, compared to the validation in buffer. This was probably caused by isocratic elution of the MVP. The validation runs showed a highly similar LRV decline for all three mAbs with mAb2 showing a decline at slightly lower counter ion concentration than mAb1 and mAb3 at both pH values. This might be caused by weak molecular interactions between MVP and mAb2. Product-specific impact of mAbs has been reported by Hung et al. hypothesizing that these impacts might be caused by hydrophilic positively charged surface patches. However, they showed as well that high counter ion concentrations reduce these effects and can therefore have a positive effect on LRVs [30]. Therefore, under high salt conditions other reasons could be responsible for the different behaviour of mAb2. The surface charge of mAb2 might impact the minimum free

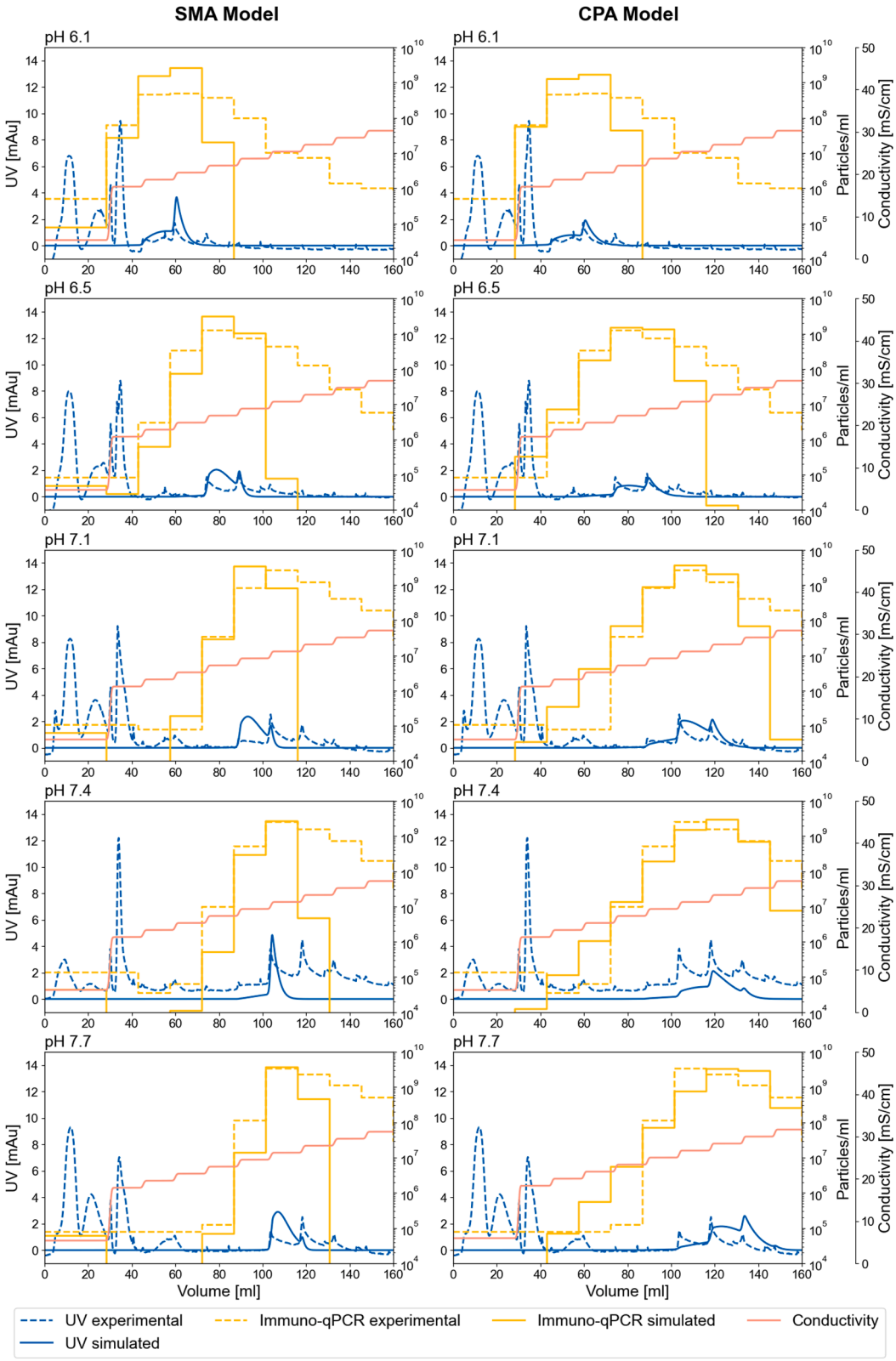

Fig. 5. Comparison of experimental and simulated chromatograms of the SMA (left) and the CPA (right) derived from the pH dependent model parameters.

interaction energy $u_{A,i}(\delta_{m,i})$, thereby limiting MVP adsorption and facilitating elution at lower counter ion concentrations. Small impact of proteins on the Donnan ratio between bulk phase and pore have been previously reported [57]. Although this impact is negligible for description of typical separation problems a small change in pore pH might become significant for prediction of LRVs. Taking into account that the predictions of both models were relatively accurate when being compared to *in silico* predicitons in literature, the edge-of-failure predictions of both models were considered as valid [32,58].

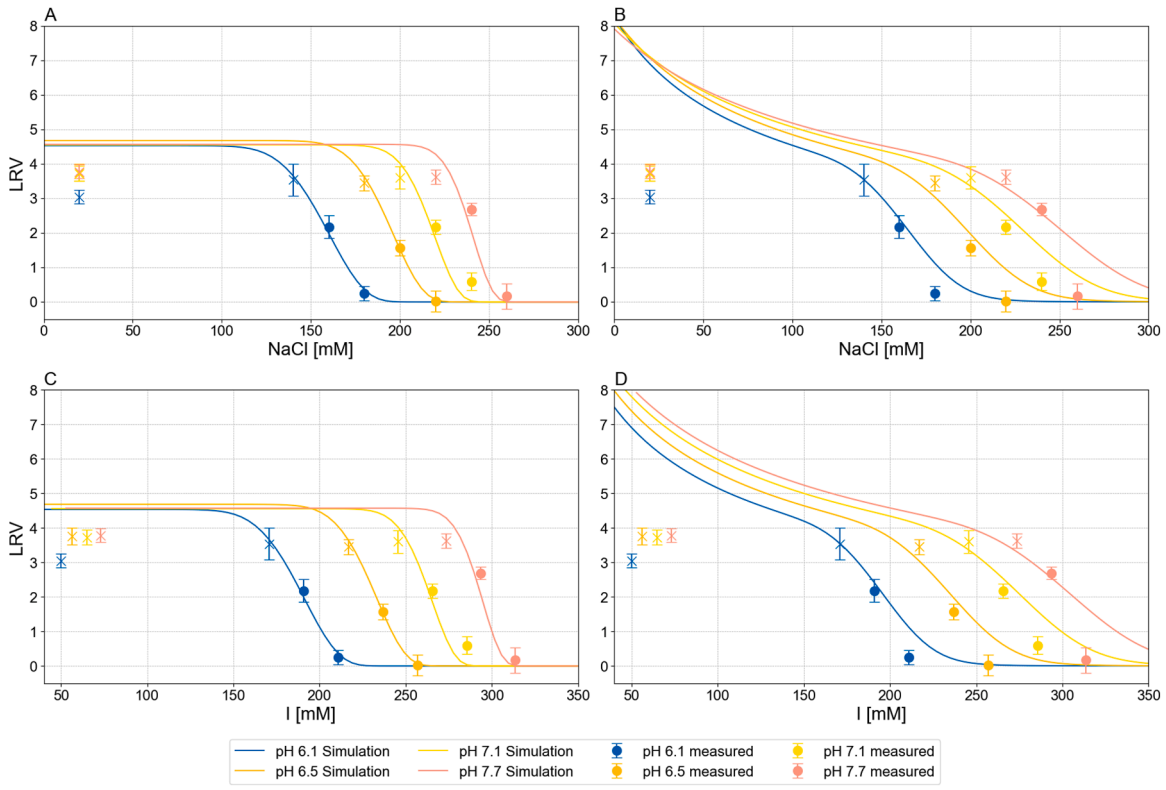

Fig. 6. Buffer validation of SMA adsorption model (A, C) and CPA adsorption model (B, D) at pH 6.1, 6.5, 7.1, and 7.7. Error bars of LRVs indicate the 95 % confidence intervals of measurements. LRVs at LOQ of the Immuo-qPCR analytics are indicated by X.

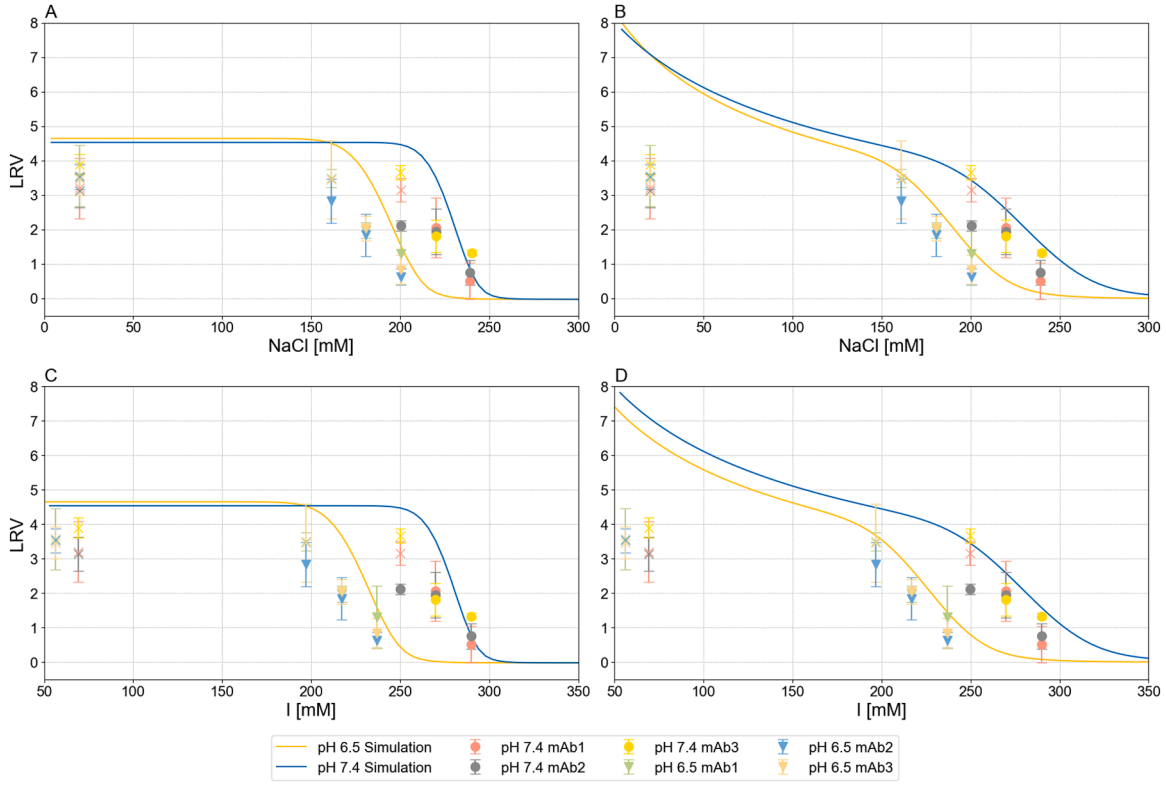

Fig. 7. mAb Validation of SMA adsorption model (A, C) and CPA adsorption model (B, D) in presence of mAb1, mAb2, and mAb 3 at pH 6.5 and 7.4. Error bars of LRVs indicate the 95 % confidence intervals of measurements. LRVs at LOQ of the Immuo-qPCR analytics are indicated by X.

Table 6
Root mean square error of prediction (RMSEP) of SMA and CPA absorption model for mAb1, mAb2, and mAb3.

	mAb1	mAb2	mAb3
LRV RMSEP SMA	1.63	2.25	1.66
LRV RMSEP CPA	0.82	1.28	0.71

4.5. Model application

After validating the edge-of-failure predictions of the CPA model in buffer and in the presence of mAbs, simulations were performed in a design space ranging from pH 6.0 – 7.8 and 0 – 300 mM of sodium chloride at the validated load volumes of 5 and 25 mL as well as extrapolations towards load volumes of 100 mL and 1000 mL (Fig. 8). Simulations of virus removal revealed an increase in counter ion resistance with rising pH. The nonlinear shape of the response surface plot might be attributed to the titration curve of the MVP. As load volumes increased, the simulations revealed a more rapid transition from effective (LRV $>$ 4) to ineffective removal (LRV $<$ 1) with rising sodium chloride concentration. However, the zone of effective removal was hardly affected by varying load volumes.

The volume dependent shift in the edge-of-failure is likely caused by weak partitioning of the MVP at increasing sodium chloride concentrations. Weak partitioning in chromatography is known to lead to delayed elution [59]. In contrast, the low impact on the effective removal zone may be explained by a sharp increase of the partitioning coefficient under these conditions, as indicated in the CPA validation plots. These findings suggest that high load volumes during AEX chromatography can influence the removal of viruses at elevated ionic strength. This might be of interest when assessing the virus removal at high volumetric loads, as commonly applied in continuous manufacturing processes [60].

5. Conclusion

In this study, we successfully used mechanistic modeling to predict the removal of a *parvovirus* MVP over a broad pH range, different ionic strengths and different load volumes. Based on the finding that the MVP used in this study has access to a certain percentage of the pore volume a GRM column model was chosen and SMA and CPA adsorption models were compared.

For the SMA model three pH-dependent parameters were necessary to describe the adsorption model, whereas the CPA model was calibrated with only the charge Z_i being pH dependent. This might enable a transfer of CPA charge Z_i to other resins and thereby reduce the calibration effort.

Both adsorption models were able to predict LRVs with reasonable accuracy. The SMA predicted a sigmoidal shape with a maximum LRV governed by the adsorption kinetics and an edge-of-failure purely described by the counter ion displacement. Although, the CPA showed a similar behavior close to the edge-of-failure, no maximum LRV but a continued increase in LRV at low ionic strength was predicted, probably caused by the dependency of kinetics on the interaction free energy. Since no residual MVPs were detected at low ionic strength (e.g. $<$ 140 mM NaCl at pH 6.1 or $<$ 220 mM NaCl at pH 7.7) it was not possible to determine which adsorption model is more accurate under these conditions. Therefore, predictions made within this parameter range should be interpreted with caution. Nevertheless, this limitation is negligible for practical applications since high removal efficiency can be expected within this experimental range. Based on literature values, the SMA predictions at low ionic strength are more likely.

Both models were well suited to predict the edge-of-failure in the presence of three different mAbs. The extrapolation of the CPA model towards higher load volumes was more accurate, which could aid the *in-silico* exploration of virus clearance behavior during continuous processing.

Although not shown in this study, it is known that weak and temporal electrostatic interactions between mAbs and *parvovirus* capsids can affect the maximum LRV of AEX [30]. A promising concept of Kitamura

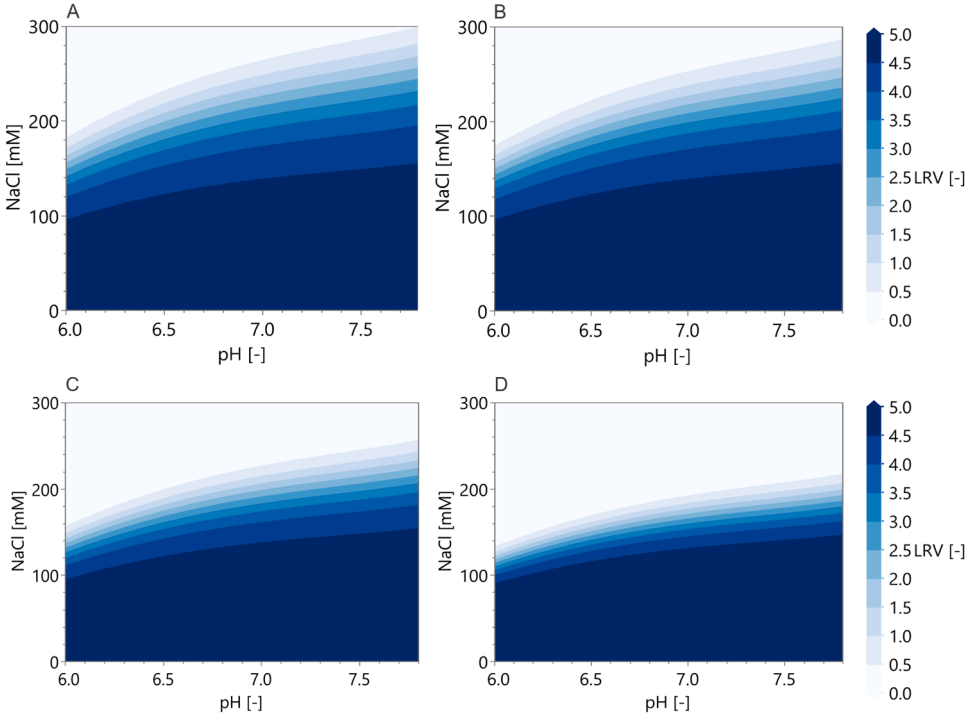

Fig. 8. Response surface plot of the effect of pH and sodium chloride combinations on the LRV of QSFF in flowthrough mode at a volumetric load of 5 mL (A), 25 mL (B), 100 mL (C), and 1000 mL (D). The plot was generated based on the validated model using a CPA adsorption isotherm.

et al. is to identify hydrophilic patches with a positive charge that have higher risks for virus mAb interactions, prior to the application of mechanistic modeling for LRV predictions [32].

In summary, both adsorption models compared were suitable to predict the edge-of-failure of MVP clearance. CPA had some major advantages over SMA. Despite leading to a better mechanistic understanding of MVP removal by AEX these findings could facilitate the mechanistic chromatography modeling of *parvoviruses* like infectious MVM, Adeno Associated Virus or other virus types (e.g. *retroviruses*). Such models could enable *in silico* risk analysis of process parameters that affect virus clearance, support of design space definition according to QbD principles and ultimately reduce the need for resource intensive viral clearance studies facilitating platform validation.

Funding

This research did not receive any specific grant from funding agencies in the public, commercial, or not-for-profit sectors.

CRediT authorship contribution statement

Lukas Döring: Writing – original draft, Software, Methodology, Investigation, Formal analysis, Data curation, Conceptualization. **Johannes Winderl:** Writing – review & editing, Validation, Supervision, Software, Methodology, Conceptualization. **Marc Müller:** Writing – original draft, Visualization, Software, Investigation. **Matthias W Kron:** Writing – review & editing, Supervision, Project administration, Funding acquisition, Conceptualization. **Jürgen Hubbuch:** Writing – review & editing, Supervision, Conceptualization.

Declaration of competing interest

The authors declare that they have no known competing financial interests or personal relationships that could have appeared to influence the work reported in this paper.

Aknowlegements

The authors would like to thank Thilo Grob, Head of Process and Analytical Science at Rentschler Biopharma for making this study possible, and the whole team for their support and the always constructive discussions.

Data availability

Data will be made available on request.

References

[1] S. Crescioli, H. Kaplon, L. Wang, J. Visweswaraiah, J.M. Reichert, S. Crescioli, H. Kaplon, L. Wang, J. Visweswaraiah, L. Wang, Antibodies to watch in 2025, MAbs 17 (2025), https://doi.org/10.1080/19420862.2024.2443538.
[2] B. Kelley, The history and potential future of monoclonal antibody therapeutics development and manufacturing in four eras, MAbs 16 (2024), https://doi.org/10.1080/19420862.2024.2373330.
[3] H. Mahal, H. Branton, S.S. Farid, End-to-end continuous bioprocessing: impact on facility design, cost of goods, and cost of development for monoclonal antibodies, Biotechnol. Bioeng. 118 (2021) 3468–3485, https://doi.org/10.1002/bit.27774.
[4] E.N. Pistikopoulos, A. Barbosa-Povoa, J.H. Lee, R. Misener, A. Mitsos, G. V. Reklaitis, V. Venkatasubramanian, F. You, R. Gani, Process systems engineering – The generation next? Comput. Chem. Eng. 147 (2021) 107252 https://doi.org/10.1016/j.compchemeng.2021.107252.
[5] S. Bhoyar, V. Kumar, M. Foster, X. Xu, S.J. Traylor, J. Guo, A.M. Lenhoff, Predictive mechanistic modeling of loading and elution in protein A chromatography, J. Chromatogr. A. 1713 (2024) 464558, https://doi.org/10.1016/j.chroma.2023.464558.
[6] T. Hahn, T. Trunzer, F. Rusly, R. Zolyomi, L.K. Shekhawat, G. Malmquist, A. Hesslein, H. Tjandra, Predictive scaling of fiber-based protein A capture chromatography using mechanistic modeling, Biotechnol. Bioeng. (2023), https://doi.org/10.1002/bit.28434.
[7] G. Sanchez-Reyes, H. Graalfs, M. Hafner, C. Frech, Mechanistic modeling of ligand density variations on anion exchange chromatography, J. Sep. Sci. 44 (2021) 805–821, https://doi.org/10.1002/jssc.202001077.
[8] R. Hess, D. Yun, D. Saleh, T. Briskot, J.H. Grosch, G. Wang, T. Schwab, J. Hubbuch, Standardized method for mechanistic modeling of multimodal anion exchange chromatography in flow through operation, J. Chromatogr. A. 1690 (2023), https://doi.org/10.1016/j.chroma.2023.463789.
[9] R. Hess, J. Faessler, D. Yun, A. Mama, D. Saleh, J.H. Grosch, G. Wang, T. Schwab, J. Hubbuch, Predicting multimodal chromatography of therapeutic antibodies using multiscale modeling, J. Chromatogr. A. 1718 (2024) 464706, https://doi.org/10.1016/j.chroma.2024.464706.
[10] D. Saleh, R. Hess, M. Ahlers-Hesse, F. Rischawy, G. Wang, J.H. Grosch, T. Schwab, S. Kluters, J. Studts, J. Hubbuch, A multiscale modeling method for therapeutic antibodies in ion exchange chromatography, Biotechnol. Bioeng. 120 (2023) 125–138, https://doi.org/10.1002/bit.28258.
[11] F. Rischawy, T. Briskot, N. Hopf, D. Saleh, G. Wang, S. Kluters, J. Studts, J. Hubbuch, Connected mechanistic process modeling to predict a commercial biopharmaceutical downstream process, Comput. Chem. Eng. 176 (2023), https://doi.org/10.1016/j.compchemeng.2023.108292.
[12] T. Briskot, N. Hillebrandt, S. Kluters, G. Wang, J. Studts, T. Hahn, T. Huuk, J. Hubbuch, Modeling the Gibbs–Donnan effect during ultrafiltration and diafiltration processes using the Poisson–Boltzmann theory in combination with a basic Stern model, J. Memb. Sci. 648 (2022), https://doi.org/10.1016/j.memsci.2022.120333.
[13] F. Rischawy, T. Briskot, F. Nitsch, D. Saleh, G. Wang, S. Kluters, J. Studts, J. Hubbuch, Modeling of biopharmaceutical UF/DF from laboratory to manufacturing scale, Comput. Chem. Eng. 177 (2023) 108337, https://doi.org/10.1016/j.compchemeng.2023.108337.
[14] P.W. Barone, M.E. Wiebe, J.C. Leung, I.T.M. Hussein, F.J. Keumurian, J. Bouressa, A. Brussel, D. Chen, M. Chong, H. Dehghani, L. Gerentes, J. Gilbert, D. Gold, R. Kiss, T.R. Kreil, R. Labatut, Y. Li, J. Müllberg, L. Mallet, C. Menzel, M. Moody, S. Monpoeho, M. Murphy, M. Plavsic, N.J. Roth, D. Roush, M. Ruffing, R. Schicho, R. Snyder, D. Stark, C. Zhang, J. Wolfrum, A.J. Sinskey, S.L. Springs, Viral contamination in biologic manufacture and implications for emerging therapies, Nat. Biotechnol. 38 (2020) 563–572. https://doi.org/10.1038/s41587-020-0507-2.
[15] E. Medicines Agency, Committee for Human Medicinal Products ICH Guideline Q5A(R2) on viral safety evaluation of biotechnology products derived from cell lines of human or animal origin step 2b, 2022. www.ema.europa.eu/contact.
[16] M. Dinowitz, Y.S. Lie, M.A. Low, R. Lazar, C. Fautz, B. Potts, J. Sernatinger, K. Anderson, Recent studies on retrovirus-like particles in Chinese hamster ovary cells, Dev. Biol. Stand. 76 (1992) 201–207. http://europepmc.org/abstract/MED/1282476.
[17] K.P. Anderson, Y.S. Lie, M.A. Low, S.R. Williams, E.H. Fennie, T.P. Nguyen, F. M. Wurm, Presence and transcription of intracisternal A-particle-related sequences in CHO cells, J. Virol. 64 (1990) 2021–2032, https://doi.org/10.1128/jvi.64.5.2021-2032.1990.
[18] C. De Wit, C. Fautz, Y. Xu, Real-time quantitative PCR for retrovirus-like particle quantification in CHO cell culture, Biologicals 28 (2000) 137–148, https://doi.org/10.1006/biol.2000.0250.
[19] M. Hussain, W.J. Rayfield, D.J. Roush, A direct RT qPCR method for quantification of retrovirus-like particles in biopharmaceutical production with CHO cells, J. Pharm. Biomed. Anal. 189 (2020), https://doi.org/10.1016/j.jpba.2020.113472.
[20] J.D. Orchard, D. Cetlin, M. Pallansch, R. Barlow, J. Borman, A. Dhar, L. Pallansch, M. Dickson, Using a noninfectious MVM surrogate for assessing viral clearance during downstream process development, Biotechnol. Prog. 36 (2020), https://doi.org/10.1002/btpr.2921.
[21] S. Johnson, K.A. Brorson, D.D. Frey, A.K. Dhar, D.A. Cetlin, Characterization of non-infectious virus-like particle surrogates for viral clearance applications, Appl. Biochem. Biotechnol. 183 (2017) 318–331, https://doi.org/10.1007/s12010-017-2447-y.
[22] R. Dyer, Y. Song, J. Chen, E. Bigelow, J. McGinnis, L. Jenkins, S. Ghose, Z.J. Li, Mechanistic insights into viral clearance during the chromatography steps in antibody processes by using virus surrogates, Biotechnol. Prog. 36 (2020), https://doi.org/10.1002/btpr.3057.
[23] C. Pan, A. Becerra-Arteaga, B. Tran, M. Chinn, H. Wang, Q. Chen, H. Lutz, M. Zhang, Characterizing and enhancing virus removal by protein A chromatography, Biotechnol. Bioeng. 116 (2019) 846–856, https://doi.org/10.1002/bit.26866.
[24] T. Kayukawa, A. Yanagibashi, T. Hongo-Hirasaki, K. Yanagida, Particle-based analysis elucidates the real retention capacities of virus filters and enables optimal virus clearance study design with evaluation systems of diverse virological characteristics, Biotechnol. Prog. 38 (2022), https://doi.org/10.1002/btpr.3237.
[25] H. Feroz, D. Cetnar, R. Hewlett, S. Sharma, M. Holstein, S. Ghose, Z.J. Li, Surrogate model to screen for inactivation-based clearance of enveloped viruses during biotherapeutics process development, Biotechnol. J. 16 (2021), https://doi.org/10.1002/biot.202100176.
[26] M.R. Brown, S.A. Johnson, K.A. Brorson, S.C. Lute, D.J. Roush, A step-wise approach to define binding mechanisms of surrogate viral particles to multi-modal anion exchange resin in a single solute system, Biotechnol. Bioeng. 114 (2017) 1487–1494, https://doi.org/10.1002/bit.26251/abstract.
[27] D.M. Strauss, T. Cano, N. Cai, H. Delucchi, M. Plancarte, D. Coleman, G.S. Blank, Q. Chen, B. Yang, Strategies for developing design spaces for viral clearance by anion exchange chromatography during monoclonal antibody production, Biotechnol. Prog. 26 (2010) 750–755, https://doi.org/10.1002/btpr.385.

[28] D.M. Strauss, S. Lute, Z. Tebaykina, D.D. Frey, C. Ho, G.S. Blank, K. Brorson, Q. Chen, B. Yang, Understanding the mechanism of virus removal by Q sepharose fast flow chromatography during the purification of CHO-cell derived biotherapeutics, Biotechnol. Bioeng. 104 (2009) 371–380, https://doi.org/10.1002/bit.22416.
[29] R. Leisi, R. Wolfisberg, T. Nowak, O. Caliaro, A. Hemmerle, N.J. Roth, C. Ros, Impact of the isoelectric point of model parvoviruses on viral retention in anion-exchange chromatography, Biotechnol. Bioeng. 118 (2021) 116–129, https://doi.org/10.1002/bit.27555.
[30] J. Hung, S.F. Lam, Z. Tan, D. Choy, N. Chennamsetty, A. Lewandowski, W. Qi, M. Lynch, S. Ghose, Z.J. Li, Impact of virus-antibody interactions on viral clearance in anion exchange chromatography, J. Chromatogr. A. 1633 (2020), https://doi.org/10.1016/j.chroma.2020.461635.
[31] L. Döring, J. Winderl, M. Kron, J. Hubbuch, Mechanistic modeling of minute virus of mice surrogate removal by anion exchange chromatography in micro scale, J. Chromatogr. A. 1734 (2024), https://doi.org/10.1016/j.chroma.2024.465261.
[32] R. Kitamura, L. Enghauser, Mechanistic model of minute virus of mice elution behavior in anion exchange chromatography purification, (2024) 1–12. https://doi.org/10.1002/btpr.3516.
[33] C.A. Brooks, S.M. Cramer, Steric mass-action ion exchange: displacement profiles and induced salt gradients, AIChE J 38 (1992) 1969–1978, https://doi.org/10.1002/aic.690381212.
[34] T. Briskot, T. Hahn, T. Huuk, J. Hubbuch, Adsorption of colloidal proteins in ion-exchange chromatography under consideration of charge regulation, J. Chromatogr. A. 1611 (2020), https://doi.org/10.1016/j.chroma.2019.460608.
[35] T. Briskot, T. Hahn, T. Huuk, J. Hubbuch, Protein adsorption on ion exchange adsorbers: a comparison of a stoichiometric and non-stoichiometric modeling approach, J. Chromatogr. A. 1653 (2021) 462397, https://doi.org/10.1016/j.chroma.2021.462397.
[36] T. Briskot, T. Hahn, T. Huuk, G. Wang, S. Kluters, J. Studts, F. Wittkopp, J. Winderl, P. Schwan, I. Hagemann, K. Kaiser, A. Trapp, S.M. Stamm, J. Koehn, G. Malmquist, J. Hubbuch, Analysis of complex protein elution behavior in preparative ion exchange processes using a colloidal particle adsorption model, J. Chromatogr. A. 1654 (2021) 462439, https://doi.org/10.1016/J.CHROMA.2021.462439.
[37] O. Lorenz-Cristea, A. Wiebe, J. Thoma, M. Veelders, T. Briskot, S. Kluters, G. Wang, D. Saleh, F. Rischawy, A systematic approach for estimating colloidal particle adsorption model parameters, J. Chromatogr. A. 1739 (2025) 465512, https://doi.org/10.1016/j.chroma.2024.465512.
[38] J. Ståhlberg, B. Jönsson, C. Horváth, Theory for electrostatic interaction chromatography of proteins, Anal. Chem. 63 (1991) 1867–1874, https://doi.org/10.1021/ac00017a036.
[39] J. Ståhlberg, B. Jönsson, Influence off charge regulation in electrostatic interaction chromatography of proteins, Anal. Chem. 68 (1996) 1536–1544, https://doi.org/10.1021/ac9509972.
[40] J. Ståhlberg, Retention models for ions in chromatography, J. Chromatogr. A. 855 (1999) 3–55, https://doi.org/10.1016/S0021-9673(99)00176-4.
[41] T.C. Huuk, T. Hahn, A. Osberghaus, J. Hubbuch, Model-based integrated optimization and evaluation of a multi-step ion exchange chromatography, Sep. Purif. Technol. 136 (2014) 207–222, https://doi.org/10.1016/j.seppur.2014.09.012.
[42] S. Hunt, T. Larsen, R.J. Todd, Modeling preparative cation exchange chromatography of monoclonal antibodies, in: A. Staby, A.S. Rathore, S. Ahuja (Eds.), Prep. Chromatogr. Sep. Proteins, Wiley, Hoboken, 2017, pp. 399–426.
[43] V.A. Parsegian, D. Gingell, Two bodies bearing unequal charges, Biophys. J. 12 (1972) 1192–1204, https://doi.org/10.1016/S0006-3495(72)86155-1.
[44] S.L. Carnie, D.Y.C. Chan, Interaction free energy between plates with charge regulation: a linearized model, J. Colloid Interface Sci. 161 (1993) 260–264, https://doi.org/10.1006/jcis.1993.1464.
[45] S.H. Behrens, M. Borkovec, Electrostatic interaction of colloidal surfaces with variable charge, J. Phys. Chem. B. 103 (1999) 2918–2928, https://doi.org/10.1021/jp984099w.
[46] G. Trefalt, S.H. Behrens, M. Borkovec, Charge regulation in the electrical double layer: ion adsorption and surface interactions, Langmuir 32 (2016) 380–400, https://doi.org/10.1021/acs.langmuir.5b03611.
[47] T.C. Huuk, T. Briskot, T. Hahn, J. Hubbuch, A versatile noninvasive method for adsorber quantification in batch and column chromatography based on the ionic capacity, Biotechnol. Prog. 32 (2016) 666–677, https://doi.org/10.1002/btpr.2228.
[48] H. Schmidt-Traub, M. Schulte, A. Seidel-Morgenstern, Separation processes chromatography - Separation of multiphase, Multicomponent Systems (2012).
[49] G. Guiochon, A. Felinger, D.G. Shirazi, A.M. Katti, Fundamentals of Preparative Chomatography, 2nd ed., Academic Press, Boston, 2006.
[50] P. DePhillips, A.M. Lenhoff, Pore size distributions of cation-exchange adsorbents determined by inverse size-exclusion chromatography, J. Chromatogr. A. 883 (2000) 39–54, https://doi.org/10.1016/S0021-9673(00)00420-9.
[51] S. Yamamoto, K. Nakanishi, R. Matsuno, T. Kamikubo, Ion exchange chromatography of proteins—Predictions of elution curves and operating conditions. II. Experimental verification, Biotechnol. Bioeng. 15 (1983) 1373–1391. http://onlinelibrary.wiley.com/doi/10.1002/bit.260250516/abstract.
[52] D. Saleh, G. Wang, B. Müller, F. Rischawy, S. Kluters, J. Studts, J. Hubbuch, Straightforward method for calibration of mechanistic cation exchange chromatography models for industrial applications, Biotechnol. Prog. 36 (2020), https://doi.org/10.1002/btpr.2984.
[53] J.A. Roberts, L. Kimerer, G. Carta, Effects of molecule size and resin structure on protein adsorption on multimodal anion exchange chromatography media, J. Chromatogr. A. 1628 (2020) 4, https://doi.org/10.1016/j.chroma.2020.4614.
[54] M.C. Stone, Y. Tao, G. Carta, Protein adsorption and transport in agarose and dextran-grafted agarose media for ion exchange chromatography: effect of ionic strength and protein characteristics, J. Chromatogr. A. 1216 (2009) 4465–4474, https://doi.org/10.1016/j.chroma.2009.03.044.
[55] T. Hahn, Advances in model-based downstream process development, Karlsruhe Institute of Technology (KIT) (2015), https://doi.org/10.5445/IR/1000051444.
[56] O.O. Ajayi, J.L. Cullinan, I. Basria, Analysis of virus clearance for biotechnology manufacturing processes from early to late phase development, 79 (2025). https://doi.org/10.5731/pdajpst.2025-000001.1.
[57] F. Wittkopp, L. Peeck, M. Hafner, C. Frech, Modeling and simulation of protein elution in linear pH and salt gradients on weak, strong and mixed cation exchange resins applying an extended Donnan ion exchange model, J. Chromatogr. A. 1545 (2018) 32–47, https://doi.org/10.1016/j.chroma.2018.02.020.
[58] H. Agarwal, X. Wang, N.R. Kulkarni, S. Tao, C. Demers, Application of machine learning in ensuring viral safety of biotherapeutics: case study demonstrating prediction and optimization of viral clearance performance of anion exchange chromatography, Curr. Res. Biotechnol. 6 (2023), https://doi.org/10.1016/j.crbiot.2023.100140.
[59] D. Iurashev, S. Schweiger, A. Jungbauer, J. Zanghellini, Dissecting peak broadening in chromatography columns under non-binding conditions, J. Chromatogr. A. 1599 (2019) 55–65, https://doi.org/10.1016/j.chroma.2019.03.065.
[60] H. Shirataki, Y. Matsumoto, F. Konoike, S. Yamamoto, Viral clearance in end-to-end integrated continuous process for mAb purification: total flow-through integrated polishing on two columns connected to virus filtration, Biotechnol. Bioeng. 120 (2023) 2977–2988, https://doi.org/10.1002/bit.28464.